

# The relation between the surface composition anomaly and the distribution of the exosphere of Mercury

Yudai Suzuki<sup>1</sup>, Kazuo Yoshioka<sup>2</sup>, Go Murakami<sup>3</sup>, and Ichiro Yoshikawa<sup>1</sup>

<sup>1</sup>University of Tokyo

<sup>2</sup>The University of Tokyo

<sup>3</sup>Japan Aerospace Exploration Agency

November 23, 2022

## Abstract

In celestial bodies with collisionless atmospheres, such as Mercury, the spatial distribution of the exosphere is expected to reflect the surface composition. In this study, we discuss whether the distribution of Mg, Ca, and Na, the primary exospheric components on Mercury, have exosphere-surface correlation (ESC) by analyzing the observation data of the Mercury Atmospheric and Surface Composition Spectrometer (MASCS) onboard the MErcury Surface, Space ENvironment, GEochemistry, and Ranging (MESSENGER) spacecraft. As a result, it was found that Mg has strong ESC, Ca has weak ESC and Na has little ESC. The Monte Carlo simulations of trajectory in the exosphere show that the weak ESC of Ca is due to the relatively large solar radiation acceleration. Na has ESC only in high-temperature regions around 0°E. This can be explained well by considering that the weakly physisorbed Na layer on the surface is depleted under high temperature and that the distribution of strongly chemisorbed Na atoms is reflected in the exosphere. Based on these results, the conditions for components with ESC in celestial bodies with thin atmospheres include low volatility and little solar radiation acceleration.

1                   **The relation between the surface composition anomaly**  
2                   **and the distribution of the exosphere of Mercury**

3 **Y. Suzuki<sup>1</sup>, K. Yoshioka<sup>1</sup>, G. Murakami<sup>2</sup>, I. Yoshikawa<sup>1</sup>**

4 <sup>1</sup> The University of Tokyo

5 <sup>2</sup> ISAS/JAXA

6 Corresponding author: Yudai Suzuki (yudai-suzuki127@g.ecc.u-tokyo.ac.jp)

7 **Key Points:**

- 8       • We discuss the correlation between Mercury's surface composition and  
9       exosphere distribution using observations by the MESSENGER spacecraft.
- 10      • Mg was found to have clear exosphere-surface correlation (ESC), Ca to have  
11      weak ESC, and Na to have little ESC.
- 12      • Conditions for components with ESC may include low volatility and small  
13      solar radiation acceleration.

14

15

**16 Abstract**

17 In celestial bodies with collisionless atmospheres, such as Mercury, the spatial distribution of the  
18 exosphere is expected to reflect the surface composition. In this study, we discuss whether the  
19 distribution of Mg, Ca, and Na, the primary exospheric components on Mercury, have  
20 exosphere-surface correlation (ESC) by analyzing the observation data of the Mercury  
21 Atmospheric and Surface Composition Spectrometer (MASCS) onboard the MErcury Surface,  
22 Space ENvironment, GEOchemistry, and Ranging (MESSENGER) spacecraft. As a result, it was  
23 found that Mg has strong ESC, Ca has weak ESC and Na has little ESC. The Monte Carlo  
24 simulations of trajectory in the exosphere show that the weak ESC of Ca is due to the relatively  
25 large solar radiation acceleration. Na has ESC only in high-temperature regions around 0°E. This  
26 can be explained well by considering that the weakly physisorbed Na layer on the surface is  
27 depleted under high temperature and that the distribution of strongly chemisorbed Na atoms is  
28 reflected in the exosphere. Based on these results, the conditions for components with ESC in  
29 celestial bodies with thin atmospheres include low volatility and little solar radiation  
30 acceleration.

31

**32 Plain Language Summary**

33 In celestial bodies with very thin atmospheres, such as Mercury, most of the atmosphere  
34 originates directly from the surface. Therefore, it can be expected that the spatial distribution of  
35 the atmosphere maintains the surface composition. In this study, we examined whether the  
36 surface distributions of Mg, Ca and Na were reflected in the atmosphere using data collected by  
37 the MASCS onboard MESSENGER. As a result, the surface distributions of Mg, Ca, and Na  
38 were clarified to be strongly, weakly, and slightly reflected in the atmosphere, respectively. A  
39 simple numerical simulation shows that the Ca atmosphere does not correspond to the surface  
40 distribution well because Ca flows in the anti-sunward direction due to high solar radiation. It  
41 was also found that the surface Na distribution is linked to the atmosphere only in high-  
42 temperature regions. In celestial bodies with thin atmospheres, components with low volatility  
43 and small resonance scattering efficiency of solar radiation may correspond well to the surface  
44 distribution.

45

## 46 1 Introduction

47 Many celestial bodies in our solar system, such as Mercury, most moons,  
48 comets, and asteroids, have a thin and collisionless atmosphere, called the  
49 exosphere. Most of these atmospheres are directly supplied from the surface  
50 through several processes such as thermal desorption, photo-stimulated desorption  
51 (PSD), charged particle sputtering, and micro-meteoroid impact vaporization (MIV).  
52 The spatial structure of the thin atmosphere strongly depends on the surface  
53 composition and energy distribution when released. Because the surface  
54 distribution of some components corresponds to geological features, it is expected  
55 that the structure of the exosphere can be directly linked to the geology. In fact, the  
56 amount of Potassium (K) exosphere on the Moon is reported to increase over the  
57 KREEP regions (Colaprete et al., 2016; Rosborough et al., 2019). The surface  
58 composition distribution and geological features of some planets with thin  
59 atmospheres may be estimated by remote atmosphere observations.

60 On Mercury, Magnesium (Mg) in the exosphere is thought to have been  
61 ejected from the surface mainly through MIV because observations by the Mercury  
62 Atmospheric and Surface Composition Spectrometer (MASCS) onboard the  
63 MErcury Surface, Space ENvironment, GEochemistry, and Ranging  
64 (MESSENGER) spacecraft show that the Mg exosphere consists of high-energy  
65 atoms and has strong dawn-dusk asymmetry (Merkel et al., 2017). The surface Mg  
66 density distribution was obtained using an X-Ray Spectrometer (XRS) onboard  
67 MESSENGER, which revealed that Mg concentrates on the terrain around 280°E  
68 in the northern hemisphere (Weider et al., 2015). Merkel et al. (2018) indicated that the  
69 production rate of the Mg exosphere should be enhanced above this Mg-rich terrain  
70 by comparing MASCS data with XRS data. This is an interesting example of  
71 exosphere-surface correlation (ESC) on Mercury identified from observations.

72 Calcium (Ca) is also mainly ejected through MIV (Burger et al., 2014). In  
73 addition, Killen and Hahn (2015) and Christou et al. (2015) suggested that the  
74 impact of comet dust streams also contributes to the ejection of Ca exosphere in  
75 some seasons. The surface Ca distribution is known to be similar to that of Mg from  
76 the observations by XRS (Weider et al., 2015; Nittler et al., 2020). Ca is expected to  
77 have ESC since Ca is a refractory component and is mainly ejected by MIV along  
78 with Mg.

79 The Sodium (Na) exosphere is known to be divided into two components: a  
80 lower-energy component ejected through PSD and a higher-energy component  
81 ejected through MIV or sputtering (Cassidy et al., 2015). Surface Na in high  
82 temperature regions has been said to be depleted due to thermal desorption, though  
83 no atoms have been detected in the exosphere ejected through thermal desorption.  
84 The seasonal variability of Na exosphere is discussed in several model study such as  
85 Mura et al. (2009) and Leblanc and Johnson (2010). Cassidy et al. (2016) found that  
86 the amount of Na exosphere is enhanced at specific “cold-pole” longitude throughout  
87 the year. They attributed this phenomenon to the fact that the maximum  
88 temperature at these longitudes is lowest on Mercury due to the rotation-revolution

89 resonance. In contrast, [Suzuki et al. \(2020\)](#) suggested that additional Na ejection  
 90 and supply of Na by dust streams' impact on these regions is also important for the  
 91 enhancement, and [Sarantos and Tsavachidis \(2020\)](#) indicates that diffusion into the  
 92 regolith also controls the amount of desorption. Although the cause of the seasonal  
 93 variability of Na exosphere still remains as a big problem, there is no doubt that  
 94 surface temperature greatly controls the amount of the exosphere throughout the  
 95 Mercury year. Thus, the surface Na distribution is highly temperature-dependent  
 96 and may not greatly reflect the geological features.

97 In summary, the current understanding predicts that Ca has clear ESC, as  
 98 does Mg, and Na has almost no ESC on Mercury. In this study, we verified whether  
 99 Mg, Ca, and Na on Mercury actually have ESC using observational data from the  
 100 MASCS and XRS to understand the relation between the distribution of the  
 101 exosphere and that of the surface composition of celestial bodies with thin  
 102 atmospheres.

103

104

## 105 2 Analysis

106 First, we deduce the production rate of the exospheric component from the  
 107 vertical profile obtained by MASCS. All the limb scan data from 2011 to 2015 were  
 108 used for the analysis. The vertical profile of Mercury's exosphere is approximated by  
 109 the Chamberlain's model ([Chamberlain, 1963](#)), as follows:

$$110 \quad N(z) = 2KH(z)\zeta n_0 \exp\left[\frac{-U(z) + U(0)}{k_B T}\right] \quad (1)$$

111 where  $z, n_0, T$  are the tangential altitude, near-surface density, and temperature,  
 112 respectively.  $2K$  is the ratio of the apparent column density to the vertical column  
 113 density, which is approximated by:

$$114 \quad 2K \sim \sqrt{\frac{2\pi(R_{Me} + z)}{H(z)}} \quad (2)$$

115  $H(z)$  is defined by the following equation, similar to scale height:

$$116 \quad H(z) = \frac{k_B T (R_{Me} + z)^2}{GM_{Me} M_{atom}} \quad (3)$$

117 where  $M_{Me}, M_{atom}, R_{Me}$  are the mass of Mercury, mass of atoms, and radius of  
 118 Mercury, respectively.  $U(z)$  is the potential of particles at altitude  $z$  expressed by the  
 119 following equations:

$$120 \quad U(z) = -\frac{GM_{Me} M_{atom}}{(R_{Me} + z)} + M_{atom} b \cos Z (R_{Me} + z) \quad (4)$$

121 where  $b, \cos Z$  are the solar radiation acceleration, and cosine of the solar zenith  
 122 angle, respectively. In equation (1),  $\zeta$  is the partition function calculated by

$$123 \quad \zeta = \frac{1}{2} + \frac{1}{2} \operatorname{erf}(\sqrt{\lambda}) - \sqrt{\frac{\lambda}{\pi}} e^{-\lambda} - \frac{\sqrt{\lambda_0^2 - \lambda^2}}{2\lambda_0} e^{-\psi} (1 + \operatorname{erf}(\sqrt{\lambda - \psi})) + \sqrt{\frac{\lambda(\lambda_0 - \lambda)}{\pi\lambda_0}} e^{-\lambda} \quad (5)$$

124 where  $\lambda, \lambda_0$  are the escape parameter at altitude  $z$  and at the surface defined as:

$$125 \quad \lambda(z) = \frac{GM_{Me}M_{atom}}{k_B T(R_{Me} + z)} \quad (6)$$

$$\lambda_0 = \frac{GM_{Me}M_{atom}}{k_B T R_{Me}}$$

126 and  $\psi$  is defined as:

$$127 \quad \psi(z) = \frac{\lambda(z)^2}{\lambda(z) + \lambda_0} \quad (7)$$

128 The Chamberlain's model does not take into account the photoionization. However,  
 129 photoionization is not effective in the observation range of MESSENGER since  
 130 typical flight scales (the product of photoionization lifetime and the thermal  
 131 velocity) of Mg, Ca and Na at a heliocentric distance of 0.4 au are, respectively,  
 132 about  $10^{6.5}$  km,  $10^{4.5}$  km and  $10^5$  km.

133 The apparent column density  $N(z)$  in  $\text{cm}^{-2}$  is derived from the observed  
 134 radiance  $4\pi I$  in Rayleigh from the following conversion formula:

$$135 \quad N (\text{cm}^{-2}) = 10^6 \frac{4\pi I}{g} \quad (8)$$

136 where  $g$  is the solar photon scattering probability (known as g-factor). The g-factor  
 137 is assumed to be uniform in a single TAA, although it originally has a standard  
 138 deviation of about 30% due to the variation depending on the radial velocity against  
 139 the Sun. The production rate  $S$  is estimated by the product of the near-surface  
 140 density and first-order moment of velocity.

$$141 \quad S = n_0 \int_0^\infty v^2 dv \int_{\theta=\frac{\pi}{2}}^{\theta=0} d \cos \theta \int_0^{2\pi} d\phi f(v, T) v \quad (9)$$

$$= \frac{n_0}{2} \sqrt{\frac{2k_B T}{\pi M_{atom}}}$$

142  $f(v, T)$  in the equation is the Maxwellian distribution.

143 We used the Levenberg-Marquardt method to estimate the near-surface  
 144 density  $n_0$  and temperature  $T$  from the vertical profile through fitting with the  
 145 model profile (Fig. 1). For Mg and Ca, because some data showed an unknown sharp

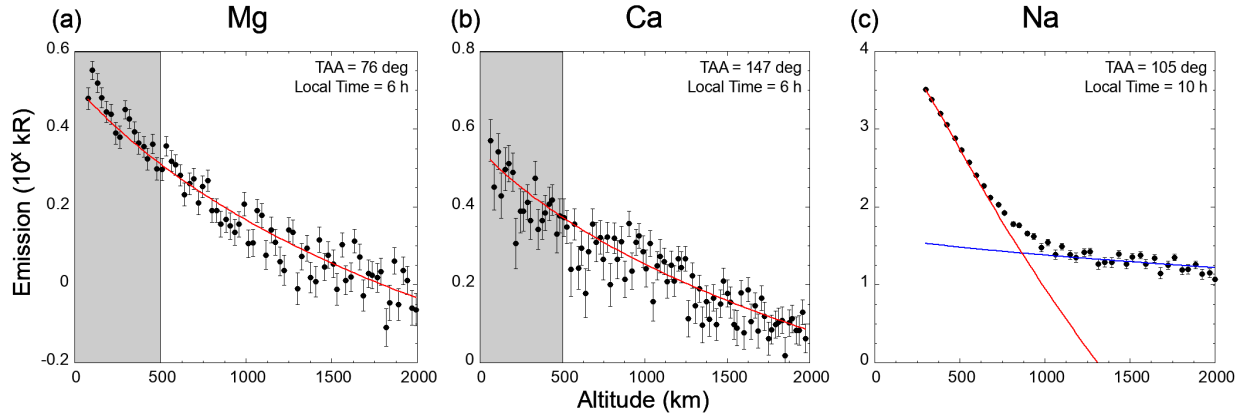


Fig. 1: Fitting to the vertical profile of (a) Mg, (b) Ca, and (c) Na.

For Mg and Ca, fitting was performed while ignoring the observations with tangential altitude is lower than 500 km (the gray region). The Na vertical profile was fitted assuming two components: a lower-energy component and a higher-energy component, and only the production rate of the lower-energy component derived from PSD was used. The Levenberg-Marquardt method was used for fitting.

146 increase in brightness at low altitudes (gray-hatched in the figure), possibly due to  
 147 uncorrected scattering from the bright surface, we used only data above 500 km for  
 148 fitting (Fig. 1(a)). For Na, because it is difficult to precisely evaluate the production  
 149 rate of higher-energy components due to the low signal to noise ratio of the data or  
 150 to the limits of the adopted physical model as pointed out in Cassidy et al. (2015),  
 151 we used only the production rate of the lower-energy component, which was ejected  
 152 through PSD (Fig. 1(b)). The production rate of Mg and Ca is comparable to the one  
 153 estimated in Merkel et al. (2017) and Burger et al. (2014), respectively.

154 To remove the effect of seasonal variability, the production rate is divided by  
 155 that at the antipodal points at the same TAA, the same local time and the different  
 156 Mercury year. Then, We defined a “relative production parameter”  $\Sigma$  at the  
 157 tangential point longitude of  $\phi$ , TAA of  $\alpha$ , and local time of  $h$ , as follows:

$$158 \quad \Sigma(\phi, \alpha, h) \equiv \log_{10} \left( \frac{S(\phi, \alpha, h)}{S(\phi + \pi, \alpha, h)} \right) \quad (10)$$

159 When calculating  $\Sigma$ , we averaged the production rate  $S$  obtained from the data for  
 160 each local time 2 h and TAA  $4^\circ$ . Since the seasonal variation is offset through this  
 161 calculation,  $\Sigma(\phi, \alpha, h)$  is expected to strongly depend on the ratio of surface  
 162 abundance. Note that  $\Sigma(\phi, \alpha, h) > 0$  means  $S(\phi, \alpha, h) > S(\phi + \pi, \alpha, h)$ , and  $\Sigma(\phi, \alpha, h) =$   
 163  $-\Sigma(\phi + \pi, \alpha, h)$ . For Mg and Ca, the correlation coefficient between  $\Sigma(\phi)$  and the  
 164 surface Mg and Ca abundance ratio,  $\log_{10}(\sigma(\phi)/\sigma(\phi + \pi))$ , where  $\sigma$  is the surface  
 165 density of Mg and Ca around the equator, is calculated. The surface density

166 distribution of Mg and Ca (Fig. 2) is derived from [Nittler et al. \(2020\)](#). Surface Na  
 167 density in the northern hemisphere was presumed by [Peplowski et al. \(2014\)](#) based  
 168 on observations by the Gamma-Ray Spectrometer (GRS) onboard MESSENGER.  
 169 However, the production rate of Na exosphere cannot be compared to the surface Na  
 170 density since the exosphere data concentrated around the equator do not spread in  
 171 the latitude direction and the surface data, on the other hand, have little  
 172 information in the longitude direction.  
 173

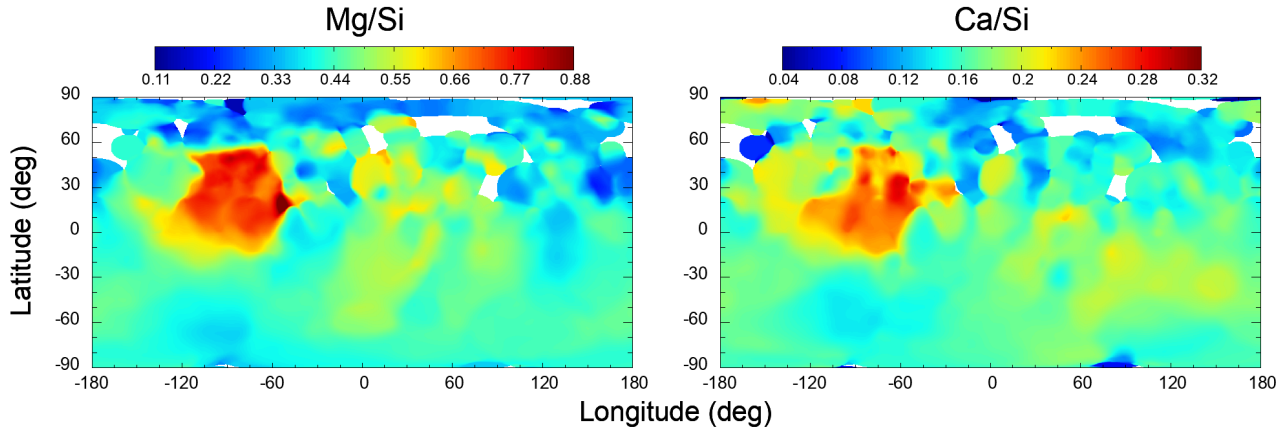


Fig. 2: The surface density distribution of (a) Mg and (b) Ca deduced from the observations by MESSENGER/XRS.

174

175

### 176 3 Results and Discussion

#### 177 3.1 Mg

178 The relative production parameters of Mg (the colored dots) and surface Mg  
 179 abundance ratio at the equator (the black solid line) as a function of longitude are  
 180 plotted in Fig. 3(a). Data points are concentrated around the  $\pm 90^\circ$  due to the  
 181 geometry of MESSENGER. In all the analyses below, including those of Ca and Na,  
 182 we have systematically removed noisy data (with relative error of  $S(\phi)/S(\phi +$   
 183  $\pi)$  greater than 10%). The correlation coefficient between the production rate ratio  
 184 and surface abundance ratio was  $r = 0.70 \pm 0.17$ , with a 95% confidence interval of  
 185  $0.65 < r < 0.76$ . The number of data used in this study was increased compared to  
 186 that of the previous study ([Merkel et al., 2018](#)), which used only local time 06 data.  
 187 In addition, calculating the surface Mg abundance ratio in the same way as the  
 188 production rate of the Mg exosphere enabled statistical tests using the correlation  
 189 coefficient, which clarifies the ESC for Mg on Mercury.

190

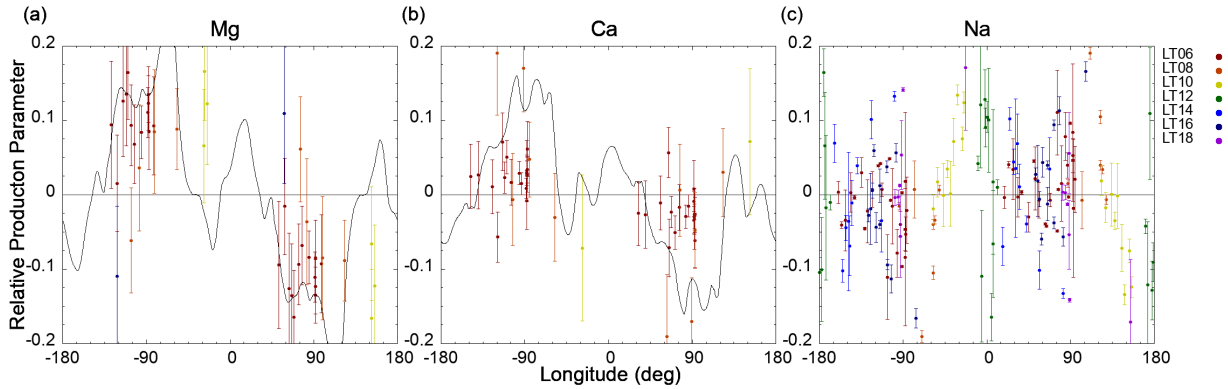


Fig. 3: The dependence of the relative production parameter on longitude.

The dot color represents the local time at which the observations were performed. The black solid line in (a) and (b) is the surface Mg abundance ratio.

191

### 192 3.2 Ca

193 The relative production parameters of Ca (the colored dots) and surface Ca  
 194 abundance ratio at the equator (the black solid line) as a function of longitude are  
 195 plotted in Fig. 3(b). The correlation coefficient between the production rate ratio and  
 196 surface abundance ratio was  $r = 0.22 \pm 0.14$ , with a 95% confidence interval of  $0.12 <$   
 197  $r < 0.32$ . This result indicates that the ESC of Ca is much weaker than that of Mg.

198 We consider that the difference between these results is due to the fact that  
 199 the g-factor of Ca is approximately ten times larger than that of Mg. As a result, Ca  
 200 experiences more solar radiation acceleration and is more likely to flow in the  
 201 tailward direction. To confirm this difference between the two components, we  
 202 performed three-dimensional Monte Carlo simulations of the trajectories of Ca and  
 203 Mg atoms in the exosphere. In this model, 10,000 atoms of Mg or Ca are ejected only  
 204 once from the point of 280°E (the red arrow), which Mg and Ca concentrate on, and  
 205 they move affected by gravity of Mercury and the Sun and solar radiation pressure.  
 206 The g-factor is set to be a function of radial velocity with respect to the Sun. We  
 207 assume that Mercury is at perihelion, or TAA = 0°. Fig. 4 shows the distribution of  
 208 Ca and Mg atoms in 60 min after ejection, seen from the south as well as the  
 209 observations by the MASCS. Killen et al. (2005) suggested that Ca is first released  
 210 as a form of CaO and dissociates into high-energy Ca atoms under UV irradiation,  
 211 while Valiev et al. (2017) showed that energetic Ca in the exosphere is not  
 212 generated from CaO. So, the source of Ca has not been identified yet. Although our  
 213 calculation used several energies in the range of 3,000K to 40,000K, the qualitative  
 214 results were the same as those in Fig. 4, which is the case of 20,000K. These results  
 215 show that information on distribution of the surface Ca is moved in the tailward by  
 216 solar radiation. This makes the ESC computationally smaller since our method

217 using Chamberlain model ignores the horizontal transport when estimating  
 218 production rate.  
 219

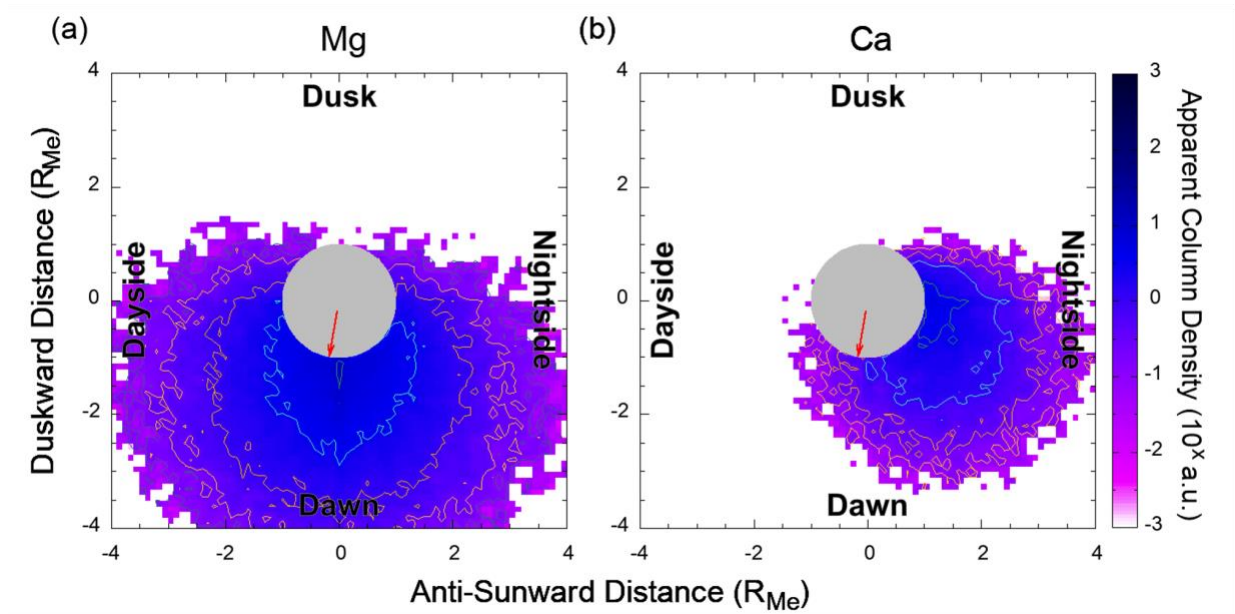


Fig. 4: Trajectories of Mg and Ca atoms using test particle simulations at perihelion. The color scale, which is displayed on a logarithmic scale, corresponds to the line-of-sight integration of the amount of the exosphere seen from the south as well as the observations by the MASCS. Note that the absolute value of the color scale does not have physical meaning. It can be seen that Ca tends to flow in the anti-sunward direction, unlike Mg.

220

221 3.3 Na

222 The relative production parameter of Na (the colored dots) as a function of  
 223 longitude is plotted in Fig. 3(c). Because Na has a larger amount of data due to its  
 224 brightness, we will discuss using only the data with relative error of  $S(\phi)/S(\phi +$   
 225  $\pi)$  is less than 5% instead of 10% (Fig. 5(a)). The relative production parameter  $\Sigma$  is  
 226 close to 0 at most longitudes, but we can see  $\Sigma > 0$  in the region of  $-45^\circ\text{E}$  to  $0^\circ\text{E}$  (red  
 227 box in Fig. 5(a)). This region has especially high maximum temperature, reaching  
 228 650K at perihelion. When we extract only the region whose temperature when the

229 data were collected is high ( $>550\text{K}$ ), we can find that  $\Sigma > 0$  in the region of  $-45^\circ\text{E}$  to  
 230  $45^\circ\text{E}$  (red box in Fig. 5(b)), which means that production rate of Na exosphere in

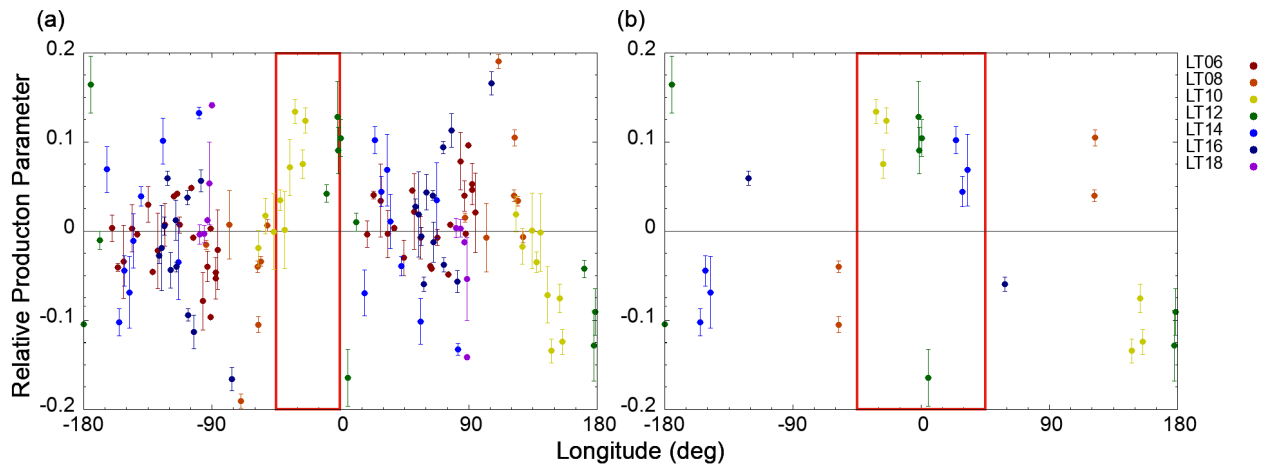


Fig. 5: The dependence of the Na relative production parameter on longitudes. (a) Data with relative error of  $S(\phi)/S(\phi + \pi)$  is less than 5% are plotted. (b) Data with relative error of  $S(\phi)/S(\phi + \pi)$  is less than 5% and with temperature above  $550\text{K}$  are plotted. The colors of each dot represents the local time when the observation was performed.

231  $45^\circ\text{E}$  to  $-45^\circ\text{E}$  is larger than in  $135^\circ\text{E}$  to  $-135^\circ\text{E}$  (Fig. 5(b)).

232 The cause of  $\Sigma > 0$  in the region of  $-45^\circ\text{E}$  to  $45^\circ\text{E}$  can be explained well by  
 233 assuming two methods of Na surface binding: physisorption and chemisorption.  
 234 Similar ideas have often been assumed in the Na exosphere models, such as the one  
 235 by [Leblanc and Johnson \(2010\)](#). Most of the physisorbed components consists of Na  
 236 atoms that re-impact the surface. Since they are easily ejected through thermal  
 237 desorption owing to their binding energy being less than  $2.0\text{ eV}$ , the distribution

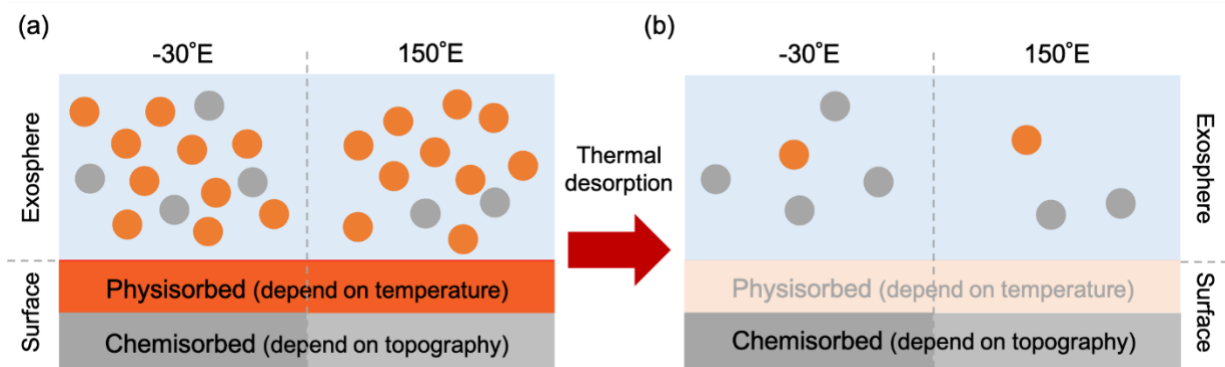


Fig. 6: A two-layer scenario of the surface Na.

(a) At the intermediate temperature of about  $500\text{ K}$ , the exosphere mainly consists of physisorbed Na atoms. (b) When the surface temperature rises, the physisorbed Na layer is depleted, and chemisorbed Na atoms occupy the exosphere. Thus, ESC is considered to appear in the extremely high-temperature regions.

238 mainly corresponds to surface temperature. In contrast, the binding energy of  
 239 chemisorbed Na atoms is approximately 2.6 eV assuming, for example, Na-O bond

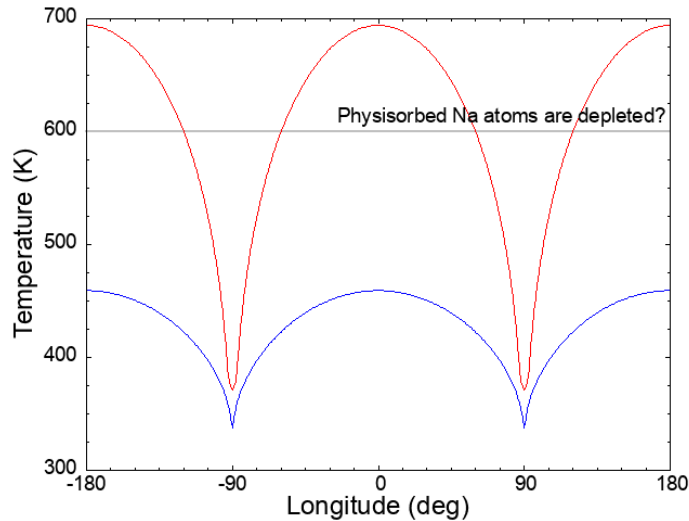


Fig. 7: The surface temperature experienced by each longitude. The red line shows the maximum temperature and the blue line shows the average temperature which each region experiences during Mercury's revolution.

240 (Bida et al., 2000), which implies chemisorbed Na are distributed depending not  
 241 only on surface temperature but on geological features.

242 The possible scenario is as follows (Fig. 6): when the surface temperature is  
 243 intermediate (lower than approximately 500K), the thermal accommodation layer,  
 244 which is composed of physisorbed atoms, is not depleted, and most of the produced  
 245 Na exosphere is derived from the physisorbed component. Therefore, the production  
 246 rate of the exosphere mainly depends on the surface temperature and UV flux.  
 247 However, in the high-temperature region above 550 K, such as around 0°E (Fig.7),  
 248 the physisorbed Na atoms are depleted by thermal desorption or diffusion into the  
 249 subsurface, and most of the ejected Na is occupied by the chemisorbed atoms. Thus,  
 250 the production rate of the exosphere also begins to depend on geological features,  
 251 that is, ESC appears in the high-temperature regions from -45°E to 45°E (and from  
 252 135°E to -135°E). Parameters related to thermal desorption, such as binding energy  
 253 and oscillation frequency, have not been determined well: [Hunten and Sprague](#)  
 254 [\(2002\)](#) adopted 1.4 eV and  $10^{13}$  Hz, [Leblanc and Johnson \(2010\)](#) used a Gaussian  
 255 distribution between 1.4 and 2.7 eV with a most probable value of 1.85 eV and  $10^9$ -  
 256  $10^{11}$  Hz, [Suzuki et al., \(2020\)](#) assumed 1.85 eV and  $10^{13}$  Hz (Fig. 8), and [Sarantos](#)  
 257 [and Tsavachidis \(2020\)](#) demonstrated that diffusion makes the energy barrier of the  
 258 desorption higher. It typically takes about 10 min for thermally desorbed atoms to  
 259 re-impact the surface. If a binding energy is less than 1.85 eV and oscillation  
 260 frequency is larger than  $10^{13}$  Hz, the desorption rate per 10 minutes reaches nearly  
 261 100 % in regions with temperature above 550 K, which is consistent with our  
 262 results. Note that the regions with larger production rate do not always correspond

263 to surface composition anomaly, since solar radiation acceleration of Na is even  
 264 larger than that of Ca. Besides, the composition anomaly of chemisorbed component  
 265 does not always reflect on the geological history of Mercury, since it also gradually  
 266 varies through repeated thermal desorption.

267

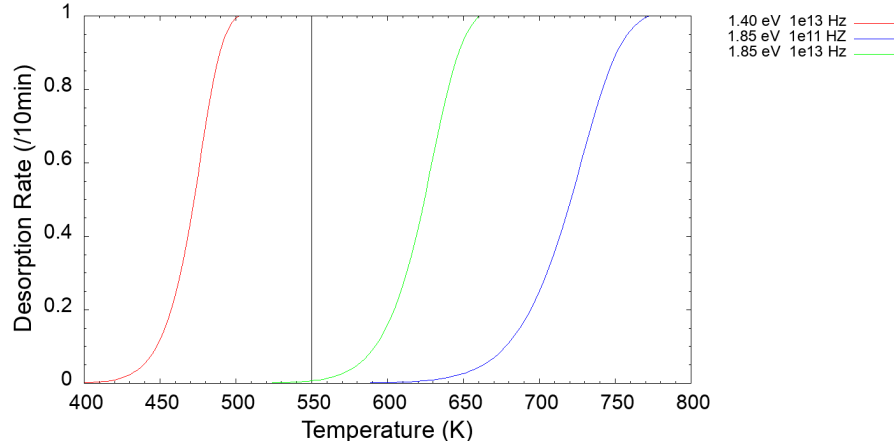


Fig. 8: Parameter dependence of the thermal desorption rate.

The red and green lines use parameter sets adopted by Hunten and Sprague (2002) and Suzuki et al., (2020), respectively. The blue line uses parameters assumed as the most probable values by Leblanc and Johnson (2010). Each line represents the proportion of thermally desorbed Na from the surface.

### 268 3.4 Implication for other components

269 From the discussion above, low volatility and small solar radiation  
 270 acceleration are important factors for ESC. Additionally, long photoionization  
 271 lifetime may also be important, although this was not found in our study.  
 272 Photoionized atoms orbit under the influence of an electromagnetic field. Since  
 273 neutral atoms with a short photoionization lifetimes in the exosphere include most  
 274 atoms that have undergone photoionization and re-neutralization, their distribution  
 275 is greatly affected by the electromagnetic field and will no longer reflect the  
 276 geological features. Therefore, a shorter photoionization lifetime is expected to  
 277 weaken ESC, except at very low altitudes. This would be verified when the  
 278 distribution of atoms with extreme short photo-ionization lifetime such as  
 279 Aluminium is observed.

280 The solar radiation acceleration and photoionization lifetimes of some of the  
 281 components of Mercury's exosphere are shown in Table 1. The solar radiation  
 282 acceleration of atoms was calculated using the following equation.

$$283 \quad b = \frac{1}{m_{atom}} \sum_i \frac{h}{\lambda_i} g_i \quad (11)$$

284 where  $m_{\text{atom}}$ ,  $h$ ,  $\lambda_i$ ,  $g_i$  are the mass of atoms, plank constant, wavelength of each  
 285 emission line, and g-factor, respectively. The g-factor was calculated using values  
 286 from Killen et al. (2009). As g-factor, that at rest and at 1 au is used. The  
 287 photoionization lifetime was derived from Fulle et al. (2007).

288 Considering the constants in Table 1, Oxygen and Sulfer have small solar  
 289 radiation acceleration and long photoionization lifetimes, which suggest existence of  
 290 ESC on Mercury. Although Na and K are more thermally desorbed, it has been  
 291 reported that the amount of Na in the Moon's exosphere increases above low-albedo  
 292 regions (Colaprete et al., 2016) and that of K is enhanced above the KREEP region  
 293 (Rosborough et al., 2019). In celestial bodies far from the central star, even atoms  
 294 that are thermally desorbed more easily, with larger solar radiation acceleration or  
 295 with shorter photoionization lifetimes, may have ESC.

Component	Solar radiation acceleration at 1 au (m/s <sup>2</sup> )	Photoionization lifetime @1 au (s)	ESC on Mercury
Na	$2.5 \times 10^{-2}$	$1.9 \times 10^5$	Little
K	$2.1 \times 10^{-4}$	$4.3 \times 10^4$	Little?
Mg	$1.9 \times 10^{-3}$	$2.1 \times 10^6$	Strong
Ca	$1.3 \times 10^{-2}$	$1.4 \times 10^4$	Weak
O	$2.5 \times 10^{-6}$	$2.0 \times 10^6$	Strong?
S	$4.4 \times 10^{-6}$	$4.2 \times 10^5$	Strong?

Table 1: The solar radiation acceleration and photoionization lifetime of each atom at 1 au.

Solar radiation acceleration is estimated using the g-factor calculated in Killen et al. (2009), and the photoionization lifetime is derived from Fulle et al. (2007). Although Na and K seem to have ESC in terms of solar radiation acceleration and photoionization, they are expected not to have ESC due to the fluctuations in surface density through thermal desorption and re-impact.

296

297

## 298 5 Conclusion

299 In celestial bodies with thin atmospheres, atoms are supplied from the  
 300 surface to the exosphere due to the effects of the space environment, such as  
 301 heating, UV radiation, and the impact of micro-meteoroids. Thus, the spatial  
 302 distribution of some components in the exosphere is expected to reflect the  
 303 distribution of each component on the surface as well as geological features such as  
 304 craters and volcanic terrain. In this study, we verified the existence of ESC on  
 305 Mercury using observations by MASCS and XRS onboard MESSENGER. As a  
 306 result, we clearly showed that Mg has strong ESC, as suggested by Merkel et al.

307 (2018), and that Ca has weak ESC. Based on simple Monte Carlo simulations, we  
 308 attributed this weak ESC of Ca to the effective tailward transportation by solar  
 309 radiation acceleration. Although Na atoms are easily desorbed thermally, it is  
 310 possible that ESC appears in the high-temperature region due to the depletion of  
 311 the physisorbed Na layer on the surface. Based on these results, we considered that  
 312 volatility and solar radiation acceleration control the ESC. S and O may also have  
 313 ESC on Mercury, and it is expected that ESC will be found in various components  
 314 on cooler celestial bodies such as Europa and Ganymede.

315 The presence or absence of ESC is a very interesting and useful issue, but  
 316 there have not been enough observational data to discuss this. We hope that  
 317 observations by the BepiColombo mission (Milillo et al., 2020; Murakami et al.,  
 318 2020), launched in 2018, will allow us to discuss this issue in more detail. This will  
 319 provide us with insights in the latitude direction — we could only discuss the  
 320 distribution in the longitude direction in this study. The MSASI (Yoshikawa et al.,  
 321 2010) onboard the Mio spacecraft will provide the detailed structure of the Na  
 322 exosphere. PHEBUS (Quémerais et al., 2020) and SERENA (Orsini et al., 2021)  
 323 onboard the MPO spacecraft will clarify the distribution of a variety of components  
 324 in the exosphere, and MERTIS (Hiesinger et al., 2020) onboard MPO will reveal a  
 325 wide range of surface material distributions on Mercury.

326

327

### 328 **Acknowledgments, Samples, and Data**

329 The original data reported in this paper are archived by Izenberg, N. (2018).  
 330 Izenberg PDART 2014 MESSENGER Advanced Products Bundle. Geosciences  
 331 Node. (<https://doi.org/10.17189/1518648>). The calculation results are archived at  
 332 <https://doi.org/10.5281/zenodo.5375947> (Suzuki et al., 2021).

333

334

### 335 **References**

336 Bida, T. A., Killen, R. M., & Morgan, T. H. (2000). Discovery of calcium in Mercury's  
 337 atmosphere. *Nature*, 404, 159-161. doi:10.1038/35004521

338 Burger, M. H., Killen, R. M., McClintock, W. E., Merkel, A. W., Vervack, R. J. Jr.,  
 339 Cassidy, T. A., & Sarantos, M. (2014). Seasonal variations in Mercury's  
 340 dayside calcium exosphere. *Icarus*, 238, 51–58.  
 341 doi:10.1016/j.icarus.2014.04.049

342 Cassidy, T. A., McClintock, W. E., Killen, R. M., Sarantos, M., Merkel, A. W.,  
 343 Vervack, R. J. Jr., & Burger, M. H. (2016). A cold-pole enhancement in

- 344 Mercury's sodium exosphere. *Geophysical Research Letters*, 43, 11,121–11,128.  
345 doi:10.1002/2016GL071071
- 346 Cassidy, T. A., Merkel, A. W., Burger, M. H., Sarantos, M., Killen, R. M.,  
347 McClintock, W. E., & Vervack, R. J. Jr. (2015). Mercury's seasonal sodium  
348 exosphere: MESSENGER orbital observations. *Icarus*, 248, 547–559.  
349 doi:10.1016/j.icarus.2014.10.037
- 350 Chamberlain, J. W. (1963). Planetary coronae and atmospheric evaporation.  
351 *Planetary and Space Science*, 11, 911–960. doi:10.1016/0032-0633(63)90122-3
- 352 Christou, A. A., Killen, R. M., & Burger, M. H. (2015). The meteoroid stream of  
353 comet Encke at Mercury: Implications for MErcury Surface, Space  
354 ENvironment, GEochemistry, and Ranging observations of the exosphere.  
355 *Geophysical Research Letters*, 42, 7311–7318. doi:10.1002/2015GL065361
- 356 Colaprete, A., Sarantos, M., Wooden, D. H., Stubbs, T. J., Cook, A. M., Shirley, M.  
357 (2016). How surface composition and meteoroid impacts mediate sodium and  
358 potassium in the lunar exosphere. *Science*, 351, 249-252.  
359 doi:10.1126/science.aad2380
- 360 Fulle, M., Leblanc, F., Harrison, R. A., Davis, C. J., Eyles, C. J., Halain, J. P.,  
361 Howard, R. A., Bockelée-Morvan, D., Cremonese, G., Scarmato, T. (2007).  
362 Discovery of the atomic iron tail of comet McNaught using the heliospheric  
363 imager on STEREO. *The Astrophysical Journal*, 661(1), L93–L96.  
364 doi:10.1086/518719
- 365 Hiesinger, H., Helbert, J., Alemanno, G., Bauch, K. E., D'Amore, M., Maturilli, A.,  
366 Morlok, A., Reitze, M. P., Stangarone, C., Sojic, A. N., Varatharajan, I., Weber,  
367 I., the MERTIS Co-I Team. (2020). Studying the Composition and Mineralogy  
368 of the Hermean Surface with the Mercury Radiometer and Thermal Infrared  
369 Spectrometer (MERTIS) for the BepiColombo Mission: An Update. *Space*  
370 *Science Review*, 216:110. doi:10.1007/s11214-020-00732-4
- 371 Hunten, D. M., & Sprague, A. L. (2002). Diurnal variation of sodium and potassium  
372 at Mercury. *Meteoritics and Planetary Science*, 37, 1191–1195.  
373 doi:10.1111/j.1945-5100.2002.tb00888.x
- 374 Izenberg, N. (2018). Izenberg PDART 2014 MESSENGER Advanced Products  
375 Bundle. Geosciences Node. doi:10.17189/1518648
- 376 Killen, R. M., Bida, T. A., & Morgan, T. H. (2005). The calcium exosphere of  
377 Mercury. *Icarus*, 173, 300-311. doi:10.1016/j.icarus.2004.08.022

- 378 Killen, R. M., & Hahn, J. M. (2015). Impact vaporization as a possible source of  
 379 Mercury's calcium exosphere. *Icarus*, 250, 230–237.  
 380 doi:10.1016/j.icarus.2014.11.035
- 381 Killen, R. M., Shemansky, D., & Mouawad, N. (2009). Expected emission from  
 382 Mercury's exospheric species, and their ultraviolet-visible signatures.  
 383 *Astrophysics Journal Supplement*, 181, 351–359. doi:10.1088/0067-  
 384 0049/181/2/351
- 385 Leblanc, F., & Johnson, R. E. (2010). Mercury exosphere I. Global circulation model  
 386 of its sodium component. *Icarus*, 209, 280–300.  
 387 doi:10.1016/j.icarus.2010.04.020
- 388 Merkel, A. W., Cassidy, T. A., Vervack, R. J. Jr., McClintock, W. E., Sarantos, M.,  
 389 Burger, M. H., & Killen, R. M. (2017). Seasonal variations of Mercury's  
 390 magnesium dayside exosphere from MESSENGER observations. *Icarus*, 281,  
 391 46–54. doi:10.1016/j.icarus.2016.08.032
- 392 Merkel, A.W., Vervack Jr., R. J., Killen, R. M., Cassidy, T. A., McClintock, W. E.,  
 393 Nittler, L. R., & Burger, M. H. (2018). Evidence Connecting Mercury's  
 394 Magnesium Exosphere to Its Magnesium-Rich Surface Terrane. *Geophysical*  
 395 *Research Letters*, 45, 6,790-6,797. doi:10.1029/2018GL078407
- 396 Milillo, A., Fujimoto, M., Murakami, G., Benkhoff, J., Zender, J., Aizawa, S., Dósa,  
 397 M., Griton, L., Heyner, D., Ho, G., Imber, S. M., Jia, X., Karlsson, T., Killen, R.  
 398 M., Laurenza, M., Lindsay, S. T., McKenna-Lawlor, S., Mura, A., Raines, J. M.,  
 399 Rothery, D. A., André, N., Baumjohann, W., Berezhnoy, A., Bourdin, P. A.,  
 400 Bunce, E. J., Califano, F., Deca, J., de la Fuente, S. Dong, C., Grava, C.,  
 401 Fatemi, S., Henri, P., Ivanovski, S. L., Jackson, B. V., James, M., Kallio, E.,  
 402 Kasaba, Y., Kilpua, E., Kobayashi, M., Langlais, B., Leblanc, F., Lhotka, C.,  
 403 Mangano, V., Martindale, A., Massetti, S., Masters, A., Morooka, M., Narita,  
 404 Y., Oliveira, J. S., Odstrcil, D., Orsini, S., Pelizzo, M. G., Plainaki, C.,  
 405 Plaschke, F., Sahraoui, F., Seki, K., Slavin, J. A., Vainio, R., Wurz, P.,  
 406 Barabash, S., Carr, C. M., Delcourt, D., Glassmeier, K. -H., Grande, M.,  
 407 Hirahara, M., Huovelin, J., Korabely, O., Kojima, H., Lichtenegger, H., Livi, S.,  
 408 Matsuoka, A., Moissl, R., Moncuquet, M., Muinonen, K., Quémenerais, E., Saito,  
 409 Y., Yagitani, S., Yoshikawa, I., Wahlund, J. -E. (2020). Investigating Mercury's  
 410 Environment with the Two-Spacecraft BepiColombo Mission. *Space Science*  
 411 *Review*, 216:93. doi:10.1007/s11214-020-00712-8
- 412 Mura, A., Wurz, P., Lichtenegger, H. I. M., Schleicher, H., Lammer, H., Delcourt,  
 413 D., Milillo, A., Orsini, S., Massetti, S., & Lhodachenko, M. L. (2009). The  
 414 sodium exosphere of Mercury: Comparison between observations during

- 415 Mercury's transit and model results. *Icarus*, 200, 1-11.  
416 doi:10.1016/j.icarus.2008.11.014
- 417 Murakami, G., Hayakawa, H., Ogawa, H., Matsuda, S., Seki, T., Kasaba, Y., Saito,  
418 Y., Yoshikawa, I., Kobayashi, M., Baumjohann, W., Matsuoka, A., Kojima, H.,  
419 Yagitani, S., Moncuquet, M., Wahlund, J. -E., Delcourt, D., Hirahara, M.,  
420 Barabash, S., Korablev, O., Fujimoto, M. (2020). Mio—First Comprehensive  
421 Exploration of Mercury's Space Environment: Mission Overview. *Space*  
422 *Science Review*, 216:113. doi:10.1007/s11214-020-00733-3
- 423 Nittler, L. R., Frank, E. A., Weider, S. Z., Crapster-Pregont, E., Vorburger, A.,  
424 Starr, R. D., Solomon, S. C. (2020) Global major-element maps of Mercury from  
425 four years of MESSENGER X-Ray Spectrometer observations. *Icarus*, 345,  
426 113716. doi: 10.1016/j.icarus.2020.113716
- 427 Orsini, S., Livi, S. A., Lichtenegger, H., Barabash, S., Milillo, A., De Angelis, E.,  
428 Phillips, M., Laky, G., Wieser, M., Olivieri, A., Plainaki, C., Ho, G., Killen, R.  
429 M., Slavin, J.A., Wurz, P., Berthelier, J.-J., Dandouras, I., Kallio, E.,  
430 McKenna-Lawlor, S., Szalai, S., Torkar, K., Vaisberg, O., Allegrini, F., Daglis,  
431 I. A., Dong, C., Escoubet, C. P., Fatemi, S., Fränz, M., Ivanovski, S., Krupp, N.,  
432 Lammer, H., Leblanc, François., Mangano, V., Mura, A., Nilsson, H., Raines,  
433 J.M., Rispoli, R., Sarantos, M., Smith, H. T., Szego, K., Aronica, A., Camozzi,  
434 F., Di Lellis, A. M., Fremuth, G., Giner, F., Gurnee, R., Hayes, J., Jeszenszky,  
435 H., Tominetti, F., Trantham, B., Balaz, J., Baumjohann, W., Brienza, D.,  
436 Bührke, U., Bush, M. D., Cantatore, M., Cibella, S., Colasanti, L., Cremonese,  
437 G., Cremonesi, L., D'Alessandro, M., Delcourt, D., Delva, M., Desai, M., Fama,  
438 M., Ferris, M., Fischer, H., Gaggero, A., Gamborino, D., Garnier, P., Gibson, W.  
439 C., Goldstein, R., Grande, M., Grishin, V., Haggerty, D., Holmström, M.,  
440 Horvath, I., Hsieh, K. -C., Jacques, A., Johnson, R. E., Kazakov, A.,  
441 Kecskemety, K., Krüger, H., Kürbisch, C., Lazzarotto, F., Leblanc, Frederic.,  
442 Leichtfried, M., Leoni, R., Loose, A., Maschietti, D., Massetti, S., Mattioli, F.,  
443 Miller, G., Moissenko, D., Morbidini, A., Noschese, R., Nuccilli, F., Nunez, C.,  
444 Paschalidis, N., Persyn, S., Piazza, D., Oja, M., Ryno, J., Schmidt, W., Scheer,  
445 J. A., Shestakov, A., Shuvalov, S., Seki, K., Selci, S., Smith, K., Sordini, R.,  
446 Svensson, J., Szalai, L., Toubanc, D., Urdiales, C., Varsani, A., Vertolli, N.,  
447 Wallner, R., Wahlstroem, P., Wilson, P., Zampieri, S. (2021). SERENA:  
448 Particle Instrument Suite for Determining the Sun-Mercury Interaction from  
449 BepiColombo. *Space Science Review*, 217:11. doi:10.1007/s11214-020-00787-3
- 450 Peplowski, P. N., Evans, L. G., Stockstill-Cahill, K. R., Lawrence, D. J., Goldsten, J.  
451 O., McCoy, T. J., Nittler, L. R., Solomon, S. C., Sprague, A. L., Starr, R. D., &  
452 Weider, S. Z. (2014). Enhanced sodium abundance in Mercury's north polar  
453 region revealed by the MESSENGER Gamma-Ray Spectrometer. *Icarus*, 228,  
454 86-95. doi:10.1016/j.icarus.2013.09.007

- 455 Quémérais, E., Chaufray, J. -Y., Koutroumpa, D., Leblanc, F., Reberac, A.,  
456 Lustrement, B., Montaron, C., Mariscal, J. -F. Rouanet, N., Yoshikawa, I.,  
457 Murakami, G., Yoshioka, K., Korablev, O., Belyaev, D., Pelizzo, M. G., Corso,  
458 A., Zuppella, P. (2020). PHEBUS on Bepi-Colombo: Post-launch Update and  
459 Instrument Performance. *Space Science Review*, 216:67. doi:10.1007/s11214-  
460 020-00695-6
- 461 Rosborough, S. A., Oliverson, R. J., Mierkiewicz, E. J., Sarantos, M., Robertson, S.  
462 D., Kurupparatchi, D. C. P., Derr, N. J., Gallant, M. A., & Roesler, F. L.  
463 (2019). High-Resolution Potassium Observations of the Lunar Exosphere.  
464 *Geophysical Research Letters*, 46, 6,964-6,971. doi:10.1029/2019GL083022
- 465 Sarantos, M., & Tsavachidis, S. (2020). The Boundary of Alkali Surface Boundary  
466 Exospheres of Mercury and the Moon. *Geophysical Research Letters*, 47(16),  
467 e2020GL088930. doi:10.1029/2020GL088930
- 468 Suzuki, Y., Yoshioka, K., Murakami, G., & Yoshikawa, I. (2020). Seasonal  
469 variability of Mercury's sodium exosphere deduced from MESSENGER data  
470 and numerical simulation. *Journal of Geophysical Research: Planets*, 125,  
471 e2020JE006472. doi:10.1029/2020JE006472
- 472 Suzuki, Y., Yoshioka, K., Murakami, G., & Yoshikawa, I. (2021). The relation  
473 between the surface composition anomaly and the distribution of the exosphere  
474 of Mercury [data set]. Zenodo. doi:10.5281/zenodo.5375947
- 475 Valiev, R. R., Berezhnoy, A. A., Sodorenko, A. D., Merzlikin, B. S., & Cherepanov, V.  
476 N. (2017). Photolysis of metal oxides as a source of atoms in planetary  
477 exospheres. *Planetary and Space Science*, 145, 38-48.  
478 doi:10.1016/j.pss.2017.07.011
- 479 Weider, S. Z., Nittler, L. R., Starr, R. D., Crapster-Pregont, E. J., Peplowski, P. N.,  
480 Denevi, B. W., Head, J. W., Byrne, P. K., Hauck II, S. A., Ebel, D. S., &  
481 Solomon, S. C. (2015). Evidence for geochemical terranes on Mercury: Global  
482 mapping of major elements with MESSENGER's X-Ray Spectrometer. *Earth  
483 and Planetary Science Letters*, 416, 109-120. doi:10.1016/j.epsl.2015.01.023
- 484 Yoshikawa, I., Korablev, O., Kameda, S., Rees, D., Nozawa, H., Okano, S., Gnedykh,  
485 V., Kottsov, V., Yoshioka, K., Murakami, G., Ezawa, F., & Cremonese, G.  
486 (2010). The Mercury sodium atmospheric spectral imager for the MMO  
487 spacecraft of Bepi-Colombo. *Planetary and Space Science*, 58(1–2), 224–237.  
488 doi:10.1016/j.pss.2008.07.008